# Remodeling of ER–plasma membrane contact sites but not STIM1 phosphorylation inhibits $Ca^{2+}$ influx in mitosis

Fang Yu[a,b], Satanay Z. Hubrack[a,b], Sumita Chakraborty[c,1], Lu Sun[a,b], Ethel Alcantara-Adap[a,b], Rashmi Kulkarni[a,b,2], Anja M. Billing[d,3], Johannes Graumann[d,4], Colin W. Taylor[c], and Khaled Machaca[a,b,5]

[a]Department of Physiology and Biophysics, Weill Cornell Medicine Qatar, Doha, Qatar, 24144; [b]Calcium Signaling Group, Weill Cornell Medicine Qatar, Doha, Qatar, 24144; [c]Department of Pharmacology, University of Cambridge, CB2 1PD Cambridge, United Kingdom; and [d]Department of Biochemistry, Weill Cornell Medicine Qatar, Doha, Qatar, 24144

Edited by Pietro De Camilli, Howard Hughes Medical Institute and Yale University, New Haven, CT, and approved April 10, 2019 (received for review December 17, 2018)

**Store-operated $Ca^{2+}$ entry (SOCE), mediated by the endoplasmic reticulum (ER) $Ca^{2+}$ sensor stromal interaction molecule 1 (STIM1) and the plasma membrane (PM) channel Orai1, is inhibited during mitosis. STIM1 phosphorylation has been suggested to mediate this inhibition, but it is unclear whether additional pathways are involved. Here, we demonstrate using various approaches, including a nonphosphorylatable STIM1 knock-in mouse, that STIM1 phosphorylation is not required for SOCE inhibition in mitosis. Rather, multiple pathways converge to inhibit $Ca^{2+}$ influx in mitosis. STIM1 interacts with the cochaperone BAG3 and localizes to autophagosomes in mitosis, and STIM1 protein levels are reduced. The density of ER–PM contact sites (CSs) is also dramatically reduced in mitosis, thus physically preventing STIM1 and Orai1 from interacting to activate SOCE. Our findings provide insights into ER–PM CS remodeling during mitosis and a mechanistic explanation of the inhibition of $Ca^{2+}$ influx that is required for cell cycle progression.**

STIM1 | mitosis | ER–PM contact sites | store-operated calcium entry | mouse knock in

Proper orchestration of the cell cycle is essential for the growth and development of multicellular organisms, with defects resulting in neoplasms and growth defects that can be fatal (1, 2). Cell cycle progression is coupled to remodeling of signaling pathways, including $Ca^{2+}$ signaling, which plays critical roles during cell division (3). $Ca^{2+}$ signals have been implicated in several stages of M phase (mitosis and meiosis), including nuclear envelope breakdown, chromosome condensation, spindle dynamics, and chromosome disjunction (4–10). The necessity for tight regulation of $Ca^{2+}$ dynamics during the cell cycle is further supported by genetic and biochemical evidence involving $Ca^{2+}$-dependent effectors, including $Ca^{2+}$-binding proteins (calmodulin), kinases (CaMKII), and phosphatases (calcineurin) (reviewed in ref. 11). The best-studied example of $Ca^{2+}$ regulating M-phase progression is at fertilization, where in all sexually reproducing species studied to date, a $Ca^{2+}$ transient triggers the egg-to-embryo transition (12). $Ca^{2+}$ signaling pathways remodel during meiosis to allow for the generation of the specialized fertilization-specific $Ca^{2+}$ signal (11). A critical component of this remodeling is the inhibition of store-operated $Ca^{2+}$ entry (SOCE) to prevent spurious $Ca^{2+}$ signals that may interfere with chromosome segregation and cell division (13).

SOCE is a ubiquitous $Ca^{2+}$ influx pathway that regulates a multitude of physiological functions ranging from secretion to immune cell activation (14, 15). $Ca^{2+}$ release from stores in response to agonists linked to G protein–coupled or tyrosine kinase receptors depletes endoplasmic reticulum (ER) $Ca^{2+}$ stores and activates SOCE through the combined action of the stromal interaction molecule (STIM) and Orai family members. STIM1 is an ER $Ca^{2+}$ sensor with luminal EF hands that oligomerizes in response to store depletion, forming clusters that then were trapped at ER–plasma membrane (PM) contact sites (CSs), initially through interactions with inositol phospholipids at ER–PM CS and then, through coupling to Orai1. Clustered STIM1 directly binds to the highly $Ca^{2+}$-selective PM channel Orai1, enriching it at ER–PM CS and gating its pore to allow for $Ca^{2+}$ influx. The gap between ER–PM junctions is ∼10–25 nm, which allows for direct STIM1–Orai1 interaction (16). In addition to assembling the SOCE machinery, recent evidence shows that ER–PM CSs also serve as platforms for regulating not only $Ca^{2+}$ dynamics but also, lipid transport and cell signaling (17–19).

SOCE is consistently down-regulated in both mitosis and meiosis (20–26), suggesting that its inhibition is essential for the progression of cell division. Indeed, overexpression of STIM1 and Orai1 during mouse meiosis partially reverses SOCE inhibition, resulting in a disruption of the egg-to-embryo transition (26). Despite the importance of SOCE inhibition in M phase, the mechanisms underlying it remain controversial and poorly defined. In meiosis, SOCE inhibition involves the internalization of Orai1 into an intracellular pool (26–28). In addition, STIM1 is unable to respond to store depletion in both meiosis and mitosis. STIM1 is phosphorylated in both frog oocyte meiosis and mitosis (25, 29) but surprisingly, is not during mouse oocyte meiosis (30).

## Significance

**The mechanisms blocking $Ca^{2+}$ influx in mitosis are complex and involve a decrease in stable endoplasmic reticulum (ER)–plasma membrane (PM) contact sites and degradation of the ER $Ca^{2+}$ sensor stromal interaction molecule 1 (STIM1) but not its phosphorylation. This challenges the current view that STIM1 phosphorylation is essential for mitotic store-operated $Ca^{2+}$ entry inhibition and sheds light on the dynamics of ER–PM contact sites and of $Ca^{2+}$ influx in mitosis.**

Author contributions: F.Y., J.G., C.W.T., and K.M. designed research; F.Y., S.Z.H., L.S., E.A.-A., R.K., and A.M.B. performed research; S.C. and C.W.T. contributed new reagents/analytic tools; F.Y., S.Z.H., L.S., E.A.-A., R.K., A.M.B., and K.M. analyzed data; and F.Y. and K.M. wrote the paper.

The authors declare no conflict of interest.

This article is a PNAS Direct Submission.



[1]Present address: Centre for Brain Development and Repair, Institute for Stem Cell Biology and Regenerative Medicine, 560065 Bengaluru, India.

[2]Present address: Integrated Group, Department of Hydroponics, Doha, Qatar, 47039.

[3]Present address: Department of Biochemistry and Molecular Biology, University of Southern Denmark, 5230 Odense, Denmark.

[4]Present address: Scientific Service Group, Biomolecular Mass Spectrometry, Max Planck Institute for Heart and Lung Research, W. G. Kerckhoff Institute Ludwigstr, D-61231 Bad Nauheim, Germany.

[5]To whom correspondence should be addressed. Email: khm2002@qatar-med.cornell.edu.

This article contains supporting information online at www.pnas.org/lookup/suppl/doi:10.1073/pnas.1821399116/-/DCSupplemental.

Published online May 7, 2019.

The C-terminal end of STIM1 contains an Ser/Thr-rich region with 10 residues that match the minimal consensus motif for the primary mitotic kinase cyclin-dependent kinase 1, Cdk1 (S/T-P). STIM1 phosphorylation has been argued to underlie SOCE inhibition in mitosis, since mutating the Ser/Thr residues to Ala (STIM1-10A) was reported to prevent the inhibition of SOCE (31). In contrast, STIM1 phosphorylation does not play a role in SOCE inhibition in oocyte meiosis based on both Ala and phosphomimetic substitutions (29). These findings suggest that STIM1 may be regulated differentially in mitosis vs. meiosis, which is surprising given the conserved kinase cascades driving M phase.

Herein, we demonstrate that phosphorylation of STIM1 is not required for SOCE suppression in mitosis. Rather, multiple processes converge to prevent SOCE during mitosis, including STIM1 degradation through the autophagy pathway and its inability to cluster in response to store depletion. Another contributing factor to inhibition of $Ca^{2+}$ influx is a dramatic reduction in ER–PM CSs in mitosis, thus physically preventing direct interaction between STIM1 and Orai1. These findings underlie a previously unrecognized complexity and highlight the evolutionary necessity to enlist redundant mechanisms to ensure complete inhibition of $Ca^{2+}$ influx in mitosis.

## Results

**SOCE Is Inhibited in Mitosis in Primary and Cultured Cells.** SOCE has been shown to be inhibited in various cultured cell lines in mitosis (20, 24, 25). We confirm SOCE inhibition in mitosis in both HEK293 and Jurkat cells using the standard protocol of depleting $Ca^{2+}$ stores with the sarcoplasmic/ER $Ca^{2+}$-ATPase (SERCA) inhibitor thapsigargin (Fig. 1 *A* and *B*). To test whether SOCE inhibition in mitosis extends to primary cells, we isolated $CD4^+$ T cells from mouse spleen and lymph nodes and expanded them under neutralizing condition ($Th_{neu}$), leading to their reentry into the cell cycle (*SI Appendix*, Fig. S1*A*). Mitotic $CD4^+$ T cells were enriched by treating with nocodazole and sorting for the G2/M-phase population (*SI Appendix*, Fig. S1*B*). SOCE was inhibited in mitotic $CD4^+$ T cells to a similar extent to what is observed in the HEK293 and Jurkat cell lines (Fig. 1*B*; *SI Appendix*, Fig. S1*C* shows enrichment of Jurkats in mitosis). To rule out potential alterations in SERCA expression or function in mitosis, we depleted stores with ionomycin and observe a similar inhibition of SOCE (*SI Appendix*, Fig. S1 *D* and *E*).

**Constitutive Activation of SOCE in Mitosis Results in Mitotic Catastrophe.** SOCE is universally inhibited in M phase, and reversing this inhibition in oocyte meiosis disrupts cell cycle progression and the egg-to-embryo transition (26). However, the effects of an active SOCE in mitosis are not known. We constitutively activated SOCE at low levels by expressing mCherry-Orai1 with the activating region from STIM1 ($Ca^{2+}$ release activated channel activation domain) (YFP-CAD) (32, 33) or YFP as a control and assessed cell viability using a membrane-impermeant dye that penetrates dead cells with damaged PM but not live cells with intact PM (*Materials and Methods*). YFP expression alone did not affect cell viability in either interphase or mitosis (Fig. 1*C*). In contrast, although SOCE activation was tolerated in interphase cells, with over 65% of the cell population surviving, it caused significant cell death of over 80% of

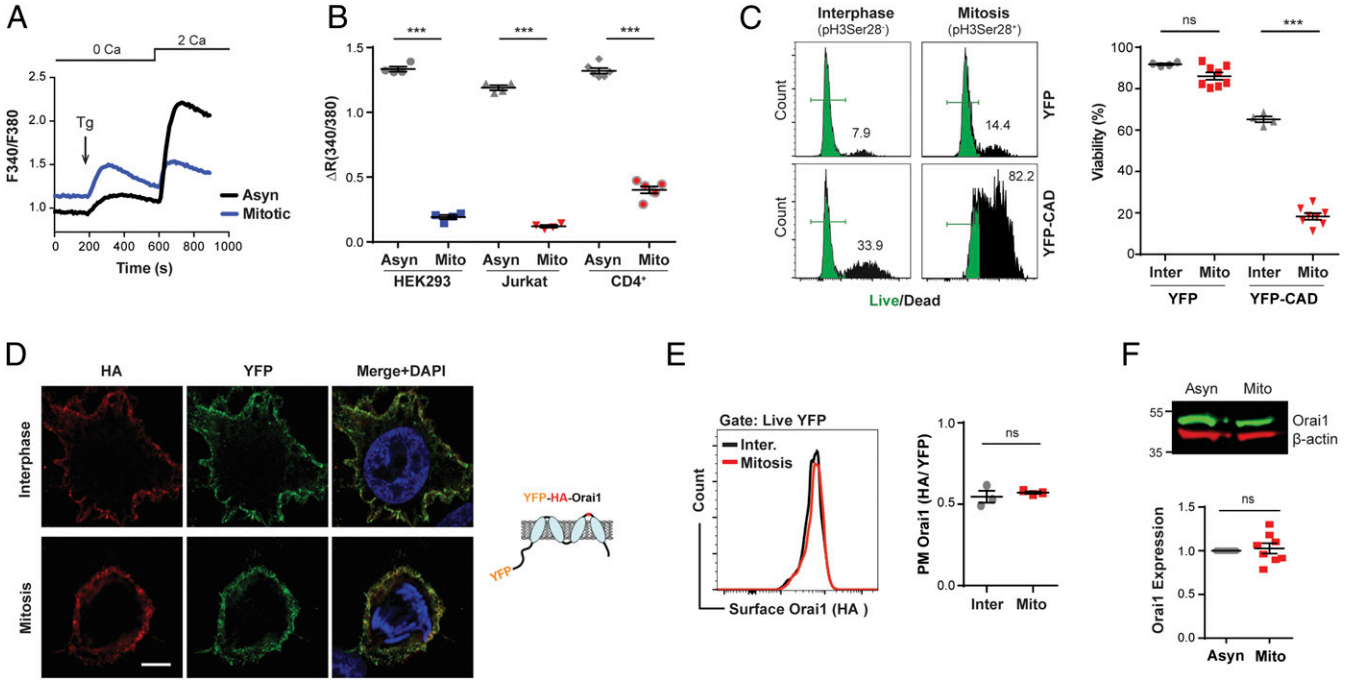


**Fig. 1.** SOCE is inhibited in mitosis, and active SOCE causes mitotic catastrophe. (*A*) Representative thapsigargin (Tg)-induced SOCE responses from asynchronous (Asyn; black) and mitotic HEK293 (Mito; blue) cells. (*B*) SOCE summary data from interphase (Inter) and mitotic (Mito) cell populations from HEK293, Jurkat, and primary $CD4^+$ T cells. SOCE was measured as the peak Fura2 ratio (F340/380) above baseline after $Ca^{2+}$ add back ($n = 4$–6; mean ± SEM, $P < 0.0001$, paired *t* test). (*C*) Constitutive SOCE causes mitotic catastrophe. SOCE was activated by coexpression of Orai1 with YFP-CAD or YFP as a control, and cell viability was assessed using a cell viability dye. Cells were also stained for pH3Ser28 to distinguish cells in mitosis ($pH3Ser28^+$) from those in interphase ($pH3Ser28^-$). Histogram distribution of live (green) and dead (black) cells in each group is shown from a representative experiment as well as the percentage viability summary data ($n = 4$–8; mean ± SEM, unpaired *t* test, $P < 0.0001$). (*D*) Representative confocal images of interphase and naturally occurring mitosis in cells stably expressing YFP-HA-Orai1. PM Orai1 was identified using anti-HA antibodies (Alexa 633) in nonpermeabilized cells, while YFP reported total cellular Orai1. Cells in interphase or mitosis were identified using DAPI (blue). (Scale bar: 5 μm.) (*E*) Flow cytometry analysis to quantify Orai1 levels at the PM ($HA^+$) in interphase (gated on $YFP^+$ $pH3Ser28^-$) and mitosis (gated on $YFP^+$ $pH3Ser28^+$). Orai1 PM levels were quantified as the ratio of HA to YFP fluorescence [$n = 3$; mean ± SEM, paired *t* test, $P \geq 0.05$ (ns)]. (*F*) Quantitative Li-COR Western blots for endogenous Orai1 expression in Asyn and Mito HEK293 cells ($n = 8$; mean ± SEM, paired Wilcoxon test, ns). ***$P \leq 0.001$.

the population in mitosis (Fig. 1*C*). This shows that a constitutively active SOCE in mitosis results in mitotic catastrophe (Fig. 1*C*), and argues that suppression of SOCE is an adaptive response that insulates mitotic cells from $Ca^{2+}$ influx to allow progression through mitosis.

**Orai1 Plasma Membrane Residence Is Not Altered in Mitosis.** Orai1 is internalized during oocyte meiosis, thus contributing to SOCE inhibition (28, 29). To assess whether Orai1 is trafficked in a similar fashion during mitosis, we measured the steady-state levels of Orai1 at the PM in mitosis compared with interphase in a cell line stably expressing Orai1 with an HA tag in the second extracellular loop and a YFP tag on the cytosolic N terminus (Fig. 1*D*, cartoon) (34). To detect PM Orai1, we stained nonpermeabilized cells with anti-HA antibodies and used DAPI to identify cells in mitosis (Fig. 1*D*). Confocal sections show Orai1 localizing to the PM in both interphase and mitosis as reported by anti-HA (Fig. 1*D*). To obtain a more quantitative measure of Orai1 levels at the PM, we used flow cytometry on nonpermeabilized cells stained with anti-HA antibodies to label PM Orai1, while total Orai1 was reported by YFP. In addition, to isolate cells in mitosis, we stained with an antiphosphorylated histone H3 at Ser28 (pH3Ser28) antibody. Histone H3 is phosphorylated in a mitosis-specific fashion and as such, distinguishes mitotic cells within the G2/M population (35). The steady-state levels of PM Orai1 estimated as the ratio of HA to YFP were indistinguishable in mitotic ($YFP^+$ $pH3Ser28^+$) and interphase ($YFP^+$ $pH3Ser28^-$) cells (Fig. 1*E*). Quantitative Western blots confirm that there was no change in Orai1 expression in mitosis (Fig. 1*F*). These results indicate that SOCE inhibition in mitosis does not involve modulation of Orai1 expression or PM residence.

**Nonphosphorylatable STIM1 Does Not Prevent Mitotic Suppression of SOCE.** We next examined the role of STIM1 phosphorylation in SOCE inhibition in mitosis. Truncation of the C-terminal end of STIM1, which contains the Cdk1 consensus sites typically phosphorylated in mitosis, or mutating to Ala the 10 Ser/Thr consensus sites has been documented to prevent SOCE inhibition in

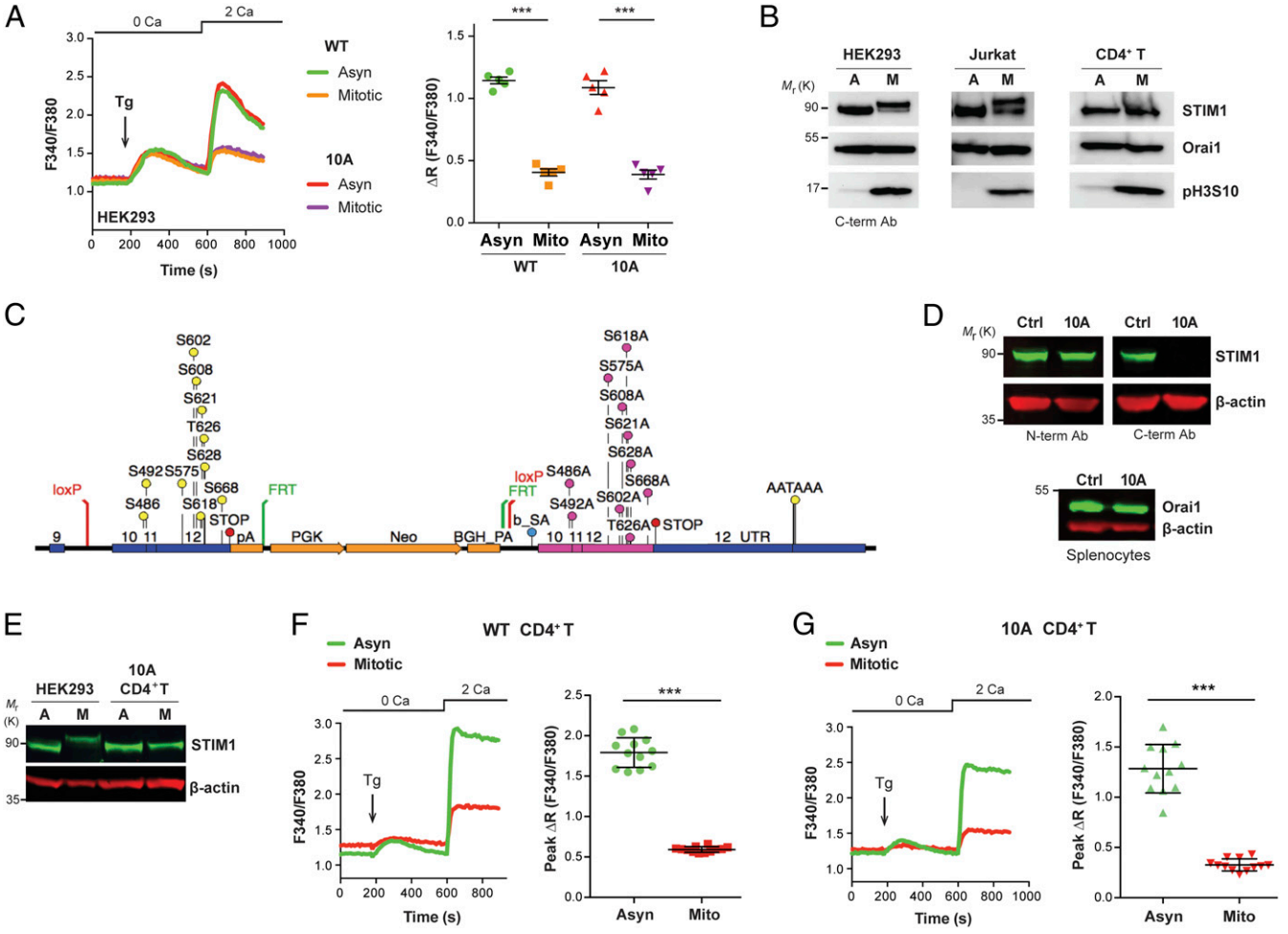


**Fig. 2.** STIM1 phosphorylation is not required for SOCE suppression in mitosis. (*A*) Representative SOCE traces from asynchronous (Asyn) and mitotic (Mito) cells transfected with mCh-STIM1 (WT) or mCh-STIM1-10A mutant (10A; *Left*). Summary data of SOCE levels (*Right*; $n = 4$; means ± SEM, paired *t* test, $P < 0.0001$ for WT and $P = 0.0006$ for 10A). Tg, thapsigargin. (*B*) Western blot analyses of STIM1, Orai1, and phosphohistone H3 (Ser10) in HEK293, Jurkat, and $CD4^+$ T cells. Representative of three similar experiments. (*C*) Schematic of the genomic region of the control STIM1-10A-KI mouse line that expresses WT STIM1. The targeting construct contained a floxed region consisting of a WT cDNA containing exons 10–12 followed by an FRT-flanked PGK promoter-driven Neo cassette upstream of the target exon coding for the S/T to A substitutions. Cre-mediated deletion replaces WT STIM1 with the 10A mutant. (*D*) Detection of endogenous STIM1 (*Top*) and Orai1 (*Bottom*) in splenocytes from control KI (Ctrl) and 10A-KI mice. STIM1 was detected using either the N-terminal Ab, which detects total STIM1, or the C-terminal mAb, which does not recognize the 10A mutant. (*E*) Western blots from asynchronous and mitotic HEK293 and $CD4^+$ T cells from the 10A-KI mice. β-actin was used as loading control. (*F* and *G*) Representative traces and summary data of SOCE in $CD4^+$ T cells from Ctrl (*F*) and 10A-KI mice (*G*; $n = 12$ from three different mice; mean ± SEM, paired *t* test, $P < 0.0001$). ***$P \leq 0.001$.

mitosis (25, 31). We, therefore, measured SOCE in cell populations expressing either WT STIM1 or the 10A mutant. In both cases, SOCE was inhibited in mitosis to similar levels (Fig. 2*A*). We confirmed that both WT STIM1 and the C-terminal truncation (STIM1-482) are functional, as they both increased SOCE levels when coexpressed with Orai1 (*SI Appendix*, Fig. S2*A*). This argues, in contrast to previous studies (25, 31), that overexpression of the nonphosphorylatable STIM1 does not prevent SOCE inhibition in mitosis.

We confirmed that the inhibition of SOCE in mitosis in cells expressing STIM1 or the 10A mutant was not due to perturbation of the STIM1–Orai1 ratio, since SOCE was also suppressed in mitosis when Orai1 was coexpressed with STIM1, the 10A mutant, or the STIM1-482 truncation (*SI Appendix*, Fig. S2 *B* and *C*). Interestingly as well, neither the 10A nor the 10E mutants were detected by the anti-STIM1 C-terminal mAb directed against the phosphorylation-rich region of STIM1 (*SI Appendix*, Fig. S3*B*; *SI Appendix*, Fig. S3 *C–E* shows additional validation of the anti-STIM1 antibodies).

**STIM1 Is Not Phosphorylated in Primary CD4$^+$ T Cells or Macrophages in Mitosis.** STIM1 from mitotic HEK293 and Jurkat cells exhibits a slower mobility on SDS/PAGE due to its phosphorylation (Fig. 2*B*). Mitosis and interphase were distinguished by the phosphorylation state of histone H3 (Fig. 2*B*). However, no shift in STIM1 electrophoretic mobility was detected in mitotic primary CD4$^+$ T cells (Fig. 2*B*) or bone marrow-derived macrophages (*SI Appendix*, Fig. S4*A*), suggesting that the phosphorylation status of mitotic STIM1 may be different in primary cells vs. cell lines. Alternatively, mouse STIM1 may not be as susceptible to the phosphorylation-induced mobility shift on SDS/PAGE, since the mobility of endogenous mouse oocyte STIM1 does not change in meiosis, while the mobility of exogenously expressed human STIM1 does (30).

To differentiate between these possibilities, we assessed STIM1 phosphorylation status and mapped phosphorylated residues on endogenous STIM1 from mitotic CD4$^+$ T cells and Jurkat cells by MS-based shotgun proteomics. Smyth et al. (25) identified S668 as the critical mitosis-specific STIM1 phosphorylation site, whereas Yu et al. (29) identified S519, S575, S618, S620/621, and S668 in meiosis. Of these sites, both S618 and S668 were phosphorylated in mitotic Jurkat cells (*SI Appendix*, Fig. S3*F*), whereas only S575 was detected in mitotic CD4$^+$ T cells (*SI Appendix*, Fig. S3*F*). Both S519 and S575 have been shown to be phosphorylated in interphase cells (25, 36). Therefore, no mitosis-specific phosphorylation of STIM1 could be detected in CD4$^+$ T cells. This in conjunction with the lack of the mobility shift associated with STIM1 phosphorylation in mitosis indicates that STIM1 is not phosphorylated in mitosis in primary CD4$^+$ T cells.

**STIM1 Phosphorylation Is Not Required for SOCE Suppression in Mitosis.** To further assess the role of STIM1 phosphorylation in mitosis in vivo, we generated an STIM1-10A–knock-in (KI) mouse strain, in which all Ser/Thr residues in the C terminus of STIM1 that match the Cdk1 consensus were substituted to Ala (Fig. 2*C*). These sites are conserved in human STIM1 (*SI Appendix*, Fig. S4*A*). The genotypes of homozygous STIM1-10A-KI and heterozygous littermate controls were confirmed by PCR (*SI Appendix*, Fig. S4*C*). Homozygous STIM1-10A-KI mice developed and reproduced normally following Mendelian ratios with no obvious growth defects or other abnormalities for over a year after reaching adulthood. This argues that STIM1 phosphorylation is not essential for the progression of either mitosis or meiosis in mice.

The nonphosphorylated STIM1-10A was expressed at similar levels to WT STIM1 in splenocytes, and it was the only expressed allele as confirmed by the anti-STIM1 C-terminal mAb (Fig. 2D), which does not detect the 10A mutant (*SI Appendix*, Fig. S3*B*). This confirms that the STIM1-10A replaced the endogenous STIM1 alleles in the STIM1-10A-KI mice. Furthermore, the expression of Orai1 was not altered in splenocytes from the STIM1-10A-KI line (Fig. 2*D*). As expected, STIM1 in mitotic CD4$^+$ T cells from the 10A-KI mice does not show the slower electrophoretic mobility observed in mitotic HEK293 cells (Fig. 2*E*).

To determine the effect of a nonphosphorylatable STIM1 on SOCE, we isolated CD4$^+$ T cells from control and STIM1-10A-KI strains and measured SOCE in interphase and mitosis. SOCE was similar in interphase CD4$^+$ T cells from WT and STIM1-10A-KI strains (*SI Appendix*, Fig. S4 *D* and *E*). Nonetheless, SOCE was suppressed to similar extents in mitotic CD4$^+$ T cells isolated from the STIM1-10A strain (inhibited by 74.33 ± 0.76%) or from the congenic control KI mouse line expressing WT STIM1 (66.65 ± 0.96%) (Fig. 2 *F* and *G*). We conclude that, even when examined at the whole-animal level, inhibition of SOCE in mitosis does not require phosphorylation of STIM1.

**STIM1 Is Down-Regulated in Mitosis.** Since SOCE inhibition in mitosis is not likely due to modulation of Orai1 or to STIM1 phosphorylation, additional mechanisms must be at play. Since proteolysis and ER remodeling have important roles in cell division, we considered whether they modulate SOCE in mitosis. We, therefore, measured STIM1 expression using quantitative Western blots in HEK293 (*SI Appendix*, Fig. S5*A*), Jurkat, and primary CD4$^+$ T cells (*SI Appendix*, Fig. S5*B*). In all three cell types, endogenous STIM1 expression decreased by ∼50% in mitosis, with no change in Orai1 protein levels (*SI Appendix*, Fig. S5*B*).

To confirm degradation of endogenous STIM1 in mitosis, we tagged one of the endogenous STIM1 alleles with EGFP using CRISPR-Cas9–mediated gene editing in HeLa cells. We refer to this cell line as STIM1-EGFP-KI. SOCE activates normally in this cell line and is suppressed in mitosis (Fig. 3*A*). Both the WT and tagged STIM1 proteins exhibit the typical mobility shift in mitosis due to phosphorylation (Fig. 3*B*). Furthermore, expression of both proteins was decreased by ∼50% in mitosis (Fig. 3*B*), supporting the conclusion that STIM1 is degraded in mitosis.

In the experiments described so far, mitotic populations were isolated after nocodazole treatment. We were concerned that prolonged arrest due to nocodazole could indirectly affect STIM1 expression. To allow identification of mitotic cells without perturbing the cell cycle, we generated an STIM1-EGFP-KI HeLa cell line that stably expresses H2B-RFP, which paints chromosomes and allows identification of mitotic cells (Fig. 3*C*). Using this line, we confirmed the loss of ∼50% of the endogenous STIM1 protein in mitosis by quantifying EGFP fluorescence (Fig. 3*C*). We further confirmed degradation of endogenous STIM1 in mitosis by stable isotope labeling of amino acids in cell culture (SILAC) labeling and quantitative MS (*SI Appendix*, Fig. S5*C*), which also showed close to a 50% decrease in STIM1 expression in mitosis. Collectively, these different approaches establish that STIM1 is degraded in a mitosis-specific fashion.

We further considered whether other proteins that contribute to ER–PM CSs (37–41) might also be degraded in mitosis. However, expressions of extended synaptotagmin 1, oxysterol-binding protein-related protein-8, and GRAM Domain Containing 2A were similar in asynchronous and mitotic cells (*SI Appendix*, Fig. S6 *D–I*). In contrast, STIM2 expression increased in mitosis (*SI Appendix*, Fig. S6 *A–C*). These data argue that STIM1 is selectively degraded in mitosis.

**Mitotic STIM1 Targets the Autophagy Pathway and Associates with the BAG3 Cochaperone.** How is STIM1 targeted for degradation during mitosis? We first explored the role of the ubiquitin–proteasome system as a well-established pivotal player in cell cycle progression. We immunoprecipitated STIM1 from asynchronous and mitotic HEK293 and Jurkat cells and from mitotic cells treated with the proteasome inhibitor MG132 (*SI Appendix*,

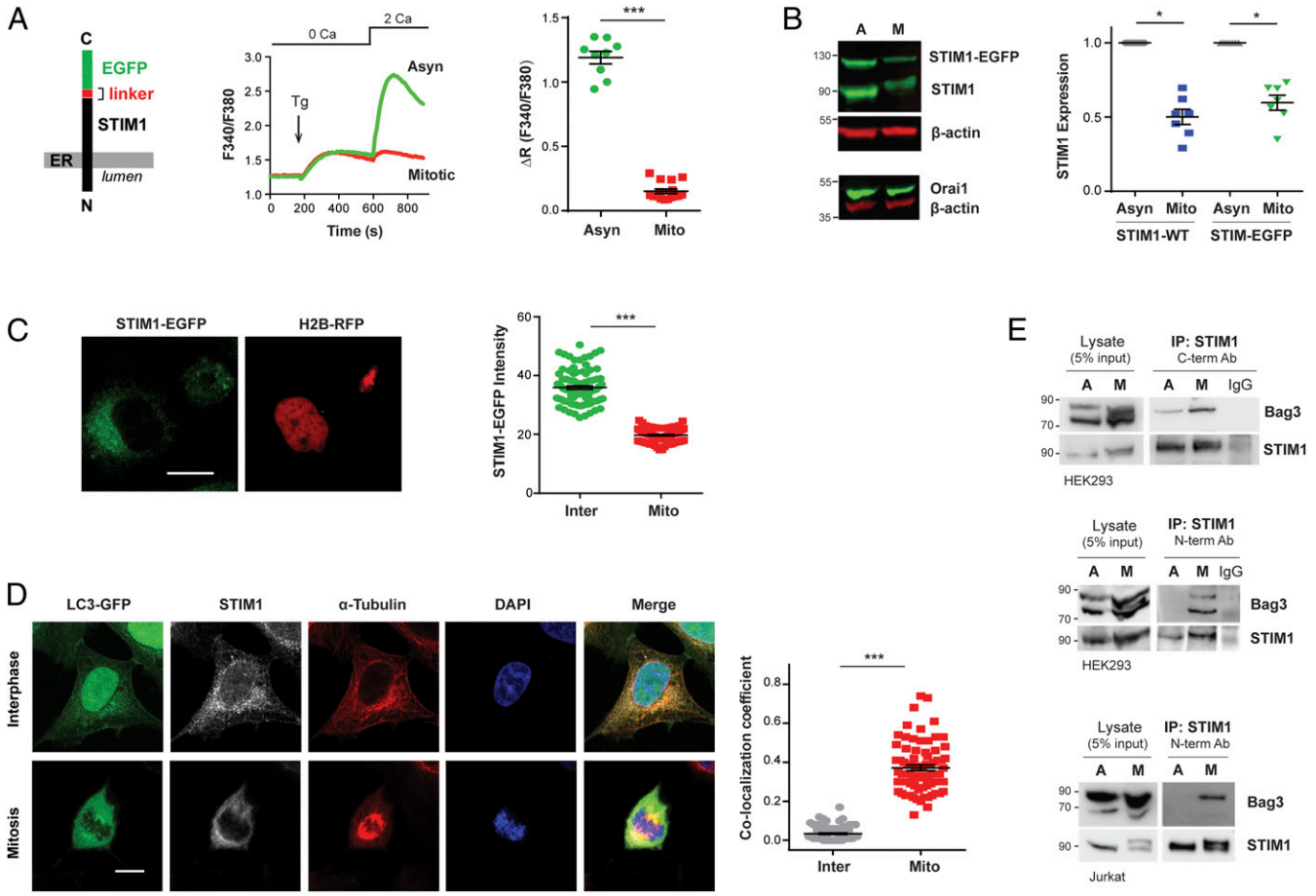


**Fig. 3.** STIM1 is down-regulated in mitosis. (*A*) Cartoon of STIM1-EGFP-KI allele with the linker sequence IKKRILQSTVPRARDPPVATMV. One allele was labeled by gene editing to tag STIM1 with EGFP (*Left*). Representative SOCE response and summary data from STIM1-EGFP-KI HeLa cells ($n$ = 9–16 wells from two independent experiments; mean ± SEM, $P < 0.0001$, unpaired $t$ test). Tg, thapsigargin. (*B*) Representative quantitative Li-COR Western blots for STIM1 and Orai1 with β-actin as the loading control, with summary data of relative protein levels (STIM1/β-actin) normalized to the levels in asynchronous (Asyn) cells for both the EGFP-tagged and WT STIM1 alleles ($n = 7$; mean ± SEM, $P = 0.0156$, Wilcoxon test). (*C*) Representative image and summary data of GFP fluorescence intensity from interphase (Inter) and mitotic (Mito) STIM1-EGFP-KI HeLa cells stably expressing H2B-RFP to visualize Mito cells ($n = 82$; mean ± SEM, $P < 0.0001$, unpaired $t$ test). (Scale bar: 10 μm.) (*D*) Colocalization of STIM1 and the autophagy marker LC3 in mitosis. Representative confocal images and quantification of STIM1 (white) localization in interphase and naturally occurring mitosis HEK293 cells stably expressing LC3-GFP (green). STIM1 was detected using the N-terminal Ab. Interphase and mitosis are indicated by the α-tubulin (red) and DAPI nuclear stain (blue). Colocalization of STIM1 and LC3 was assessed using the Pearson coefficient ($n$ = 77–84 from two independent experiments; mean ± SEM, $P < 0.0001$, unpaired $t$ test). (*E*) Endogenous STIM1 interacts with BAG3 in mitotic cells. DSP cross-linked Asyn and Mito HEK293 lysates were immunoprecipitated with either STIM1 C-terminal Ab (HEK; *Top*) or N-terminal Ab [HEK (*Middle*) and Jurkat (*Bottom*)]. Western blots analysis with BAG3 and STIM1 antibodies shows preferential interaction in mitosis. Images are representative of two independent experiments. IP, immunoprecipitation. $^*P < 0.05$; $^{***}P \leq 0.001$.

Fig. S7*A*). As expected, MG132 treatment in mitosis increased the levels of ubiquitinated proteins (*SI Appendix*, Fig. S7*A*). However, there is no discernable increase in STIM1 polyubiquitination in mitosis independent of MG132 treatment (*SI Appendix*, Fig. S7*A*), arguing that proteasomal degradation is not involved in STIM1 degradation in mitosis. Consistent with a previous report (42), we did detect monoubiquitinated STIM1 in interphase as well as in mitosis (*SI Appendix*, Fig. S7*A*).

Selective autophagy also plays important roles in mitosis (43). We, therefore, tested whether STIM1 is targeted to autophagosomes in mitosis. We imaged the distribution of endogenous STIM1 and the autophagosome marker LC3 in asynchronous and mitotic HEK293 cells stably expressing LC3-GFP (Fig. 3*D*). Pearson colocalization analysis show a high colocalization index in mitosis but not in interphase cells (Fig. 3*D*), implying that STIM1 targets to autophagosomes in mitosis. Inhibition of autophagy using bafilomycin $A_1$ (44) prevented STIM1 degradation in mitosis (*SI Appendix*, Fig. S7*B*).

To further assess the mechanisms targeting STIM1 to autophagosomes in mitosis, we focused on the cochaperone BAG3, which plays a critical role in mitosis progression by targeting proteins for selective autophagy (45, 46). We show that STIM1 interacts preferentially with BAG3 in mitosis. STIM1 pulldown experiments with multiple antibodies show increased STIM1 with BAG3 in mitosis in both HEK293 and Jurkat cells (Fig. 3*E*). Furthermore, quantitative MS analysis of SILAC-labeled endogenous proteins shows an ∼30% increase in BAG3 expression in mitosis (*SI Appendix*, Fig. S4*C*). These results suggest that BAG3 preferentially binds to STIM1 in mitosis and targets it to autophagosomes for degradation.

**STIM1 Does Not Form Stable Clusters After Store Depletion in Mitosis.** STIM1 down-regulation would contribute to SOCE inhibition, but it is not sufficient, since STIM1 overexpression does not rescue SOCE in mitosis. We, therefore, tested the ability of endogenous STIM1 to cluster in mitosis. STIM1 oligomerization and the stoichiometry of STIM1–Orai1 clusters are affected by the levels of expression of STIM1 (34, 47). We, therefore, took

care to visualize STIM1 clusters only in cells expressing endogenous or near-endogenous levels of STIM1. In response to store depletion with either thapsigargin (Fig. 4*A*) or ionomycin (*SI Appendix*, Fig. S7*B*), STIM1 clusters and forms stable puncta in interphase but not in mitosis in STIM1-EGFP-H2B-RFP HeLa cells. To corroborate this finding, we generated a stable cell line expressing human STIM1-YFP using STIM1-knockout mouse embryonic fibroblast (MEF) cells (48) such that the only STIM1 expressed is the YFP-tagged version. In this case as well, store depletion leads to STIM1 puncta formation in interphase but not mitotic cells (Fig. 4*B*). These results show that STIM1 does not form stable puncta in response to store depletion in mitosis. Consistent with these findings, overexpressed STIM1 was shown not to form puncta in response to store depletion in oocyte meiosis and in mitosis (25, 29).

**ER–PM Junctions Are Down-Regulated During Mitosis.** Mitosis is associated with remodeling of the cytoskeleton and organelles, including the ER (49). Furthermore, mitotic cells have increased internal hydrostatic pressure and surface tension that drive cell rounding, which is important for spindle orientation and chromosome segregation (50). We expressed GFP-membrane-attached peripheral ER (MAPPER), a well-characterized probe for ER–PM junctions that does not discernably modify them (51), in H2B-RFP stable HEK293 cells to identify mitotic cells (Fig. 4*C*). As expected, MAPPER localizes in a punctate pattern—indicative of ER–PM CS—preferentially at the PM focal plane compared with the cell equator in interphase cells (Fig. 4*C*). In contrast, GFP-MAPPER is diffusely distributed in mitotic cells (Fig. 4*C*). A 3D reconstruction of the cell volume with punctate GFP-MAPPER pseudocolored as gray dots and diffuse MAPPER in green in Fig. 4*D*, highlights the loss of ER–PM CS in mitosis (Fig. 4*D*). Quantification of the density of ER–PM CS marked by MAPPER shows a 16-fold decrease in mitosis: 0.178 ± 0.010 puncta per 1 $\mu m^3$ in interphase vs. 0.011 ± 0.002 puncta per 1 $\mu m^3$ in mitosis (Fig. 4*E*). Combined total internal reflection fluorescence (TIRF) and epifluorescence imaging of GFP-MAPPER distribution in the same cells confirms the loss of ER–PM CS in mitosis (*SI Appendix*, Fig. S7*D*).

A version of MAPPER with a shorter cytosolic linker (*SI Appendix* has details) reveals a similar down-regulation of ER–PM CS in mitosis (*SI Appendix*, Fig. S8). This shows that the length of



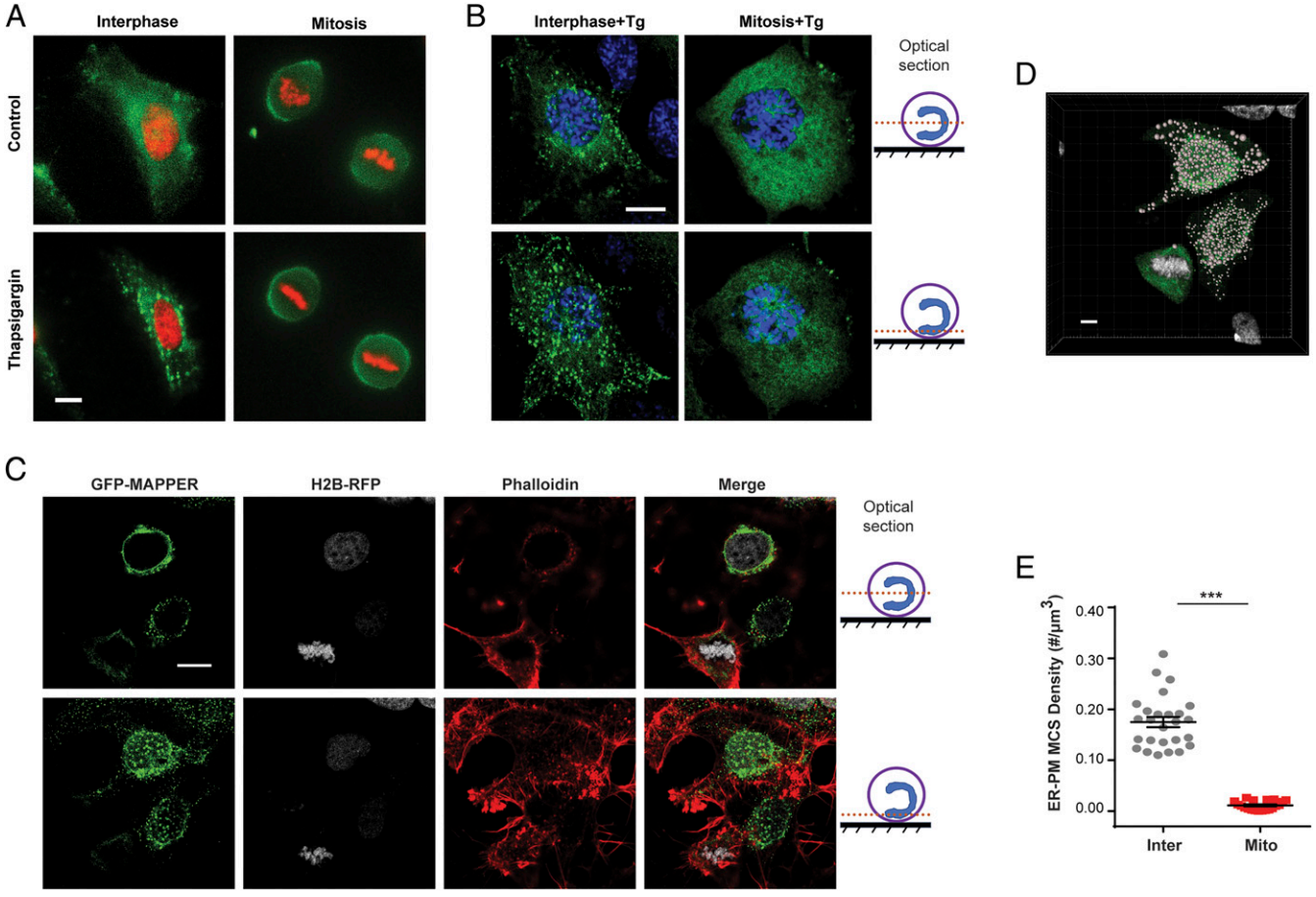


**Fig. 4.** ER–PM CSs are down-regulated in mitosis. (*A*) Representative epifluorescence images from live interphase and mitotic STIM1-EGFP-KI HeLa cells stably expressing H2B-RFP at rest (Control) or after store depletion with thapsigargin (Tg; representative of 20 similar fields imaged from three different experiments). (*B*) Confocal images of interphase and mitotic STIM1-knockout MEF cells stably expressing hSTIM1-YFP (green) after store depletion with Tg. Interphase and mitosis are indicated by DAPI staining (blue). Two different optical sections are shown: at the coverslip plane to visualize the cell cortex and through the middle of the cell (representative of 20 similar fields from three independent experiments). (*C*) Confocal images of ER–PM junctions as indicated by GFP-MAPPER in interphase and mitotic H2B-RFP (white) stable HEK293 cells. Cells were also stained with phalloidin to visualize F-actin (Alexa 633; red). Two different optical sections are shown at the coverslip plane and through the middle of the cell (representative of 20 similar fields imaged from three independent experiments). (Scale bar: 10 μm.) (*D*) A 3D rendition through the volume of the cells shown in *C*, with the actin staining removed for clarity. ER–PM CSs are shown in gray with diffuse intracellular MAPPER in green. (*E*) Quantification of ER–PM CS density in interphase and mitotic cells ($n$ = 20–26 from three independent experiments; mean ± SEM, $P < 0.0001$, unpaired $t$ test). ***$P \leq 0.001$.

the linker, which would be expected to bring the ER and PM closer together (51), has no bearing on the loss of ER–PM CS in mitosis. Collectively, these results argue that ER remodeling in mitosis is associated with loss of ER–PM CSs.

We also assessed ER–PM CS remodeling at the ultrastructural level in Jurkat cells by EM on sections near the cell equator. We identified interphase cells by their diffuse DNA and intact nuclear envelope and mitotic cells by their condensed chromosomes and absence of a nuclear envelope (Fig. 5 *A* and *B*). We defined ER–PM CS as areas where the distance between the ER and PM was ≤30 nm. The density of ER–PM CS was significantly reduced in mitosis (0.098 ± 0.012 in interphase to 0.02 ± 0.0027 in mitosis) (Fig. 5*C*). Even when present, ER–PM CSs were slightly but significantly wider in mitosis (19.37 ± 0.57 nm, $n = 117$) compared with interphase (17.4 ± 0.36 nm, $n = 346$) (Fig. 5*D*). Furthermore, ER–PM CSs were, on average, longer in interphase (122.8 ± 5.7 nm) than during mitosis (99.17 ± 7 nm) (Fig. 5*E*) due primarily to the loss of long ER–PM CS (>300 nm) in mitosis (Fig. 5*E*). These analyses show that, in addition to the significant reduction in the number of ER–PM CS in mitosis, those that remain are shorter and wider.

Interestingly, ER–PM CSs in interphase were of two distinct classes based on the orientation of the ER toward the PM, with the ER tubule either running parallel to the PM or approaching the PM at an angle (Fig. 5*A*). In mitosis, the ER invariably was oriented parallel to the PM (Fig. 5*B*).

We also measured distances between the PM and the closest ER tubule, which for interphase cells, represents the ER–PM CS (Fig. 5*F*). In mitosis, most sections lacked ER–PM CS, with ER tubules instead appearing fragmented, consistent with remodeling of the ER. Most of these near-PM ER tubules run parallel to the PM but at some distance from it (103.5 + 2.65 nm, $n = 775$) (Fig. 5*B*, arrowheads), with only a small portion coming close enough to the PM to create an ER–PM CS in mitosis (Fig. 5*B*, arrows). Therefore, most ER in mitotic cells is too far from the PM to allow for direct STIM1–Orai1 interactions and SOCE.

## Discussion

Cells have evolved mechanisms to remodel $Ca^{2+}$ signals during cell division to ensure genomic and cell cycle integrity. A conserved aspect of this regulation is the inhibition of SOCE to allow cell division to proceed. Indeed, constitutive low-level activation of SOCE, although well tolerated in interphase, causes mitotic catastrophe (Fig. 1*C*). Herein, we elucidate multiple mechanisms that combine to effectively inhibit SOCE in mitosis and resolve a long-standing controversy in the field by showing that this inhibition does not involve STIM1 phosphorylation.

Based in part on overexpression of nonphosphorylatable STIM1 mutants, STIM1 phosphorylation was argued to be sufficient to inhibit SOCE in mitosis (25, 31). We were unable to replicate these findings (Fig. 2*A* and *SI Appendix*, Fig. S2). One potential technical discrepancy is that, in the previous studies, mitotic cells were identified based on cell rounding, which may include cells at the G2/M transition not yet committed to mitosis, thus skewing the results toward functional SOCE. Furthermore, the phosphorylation state of STIM1 does not correlate with

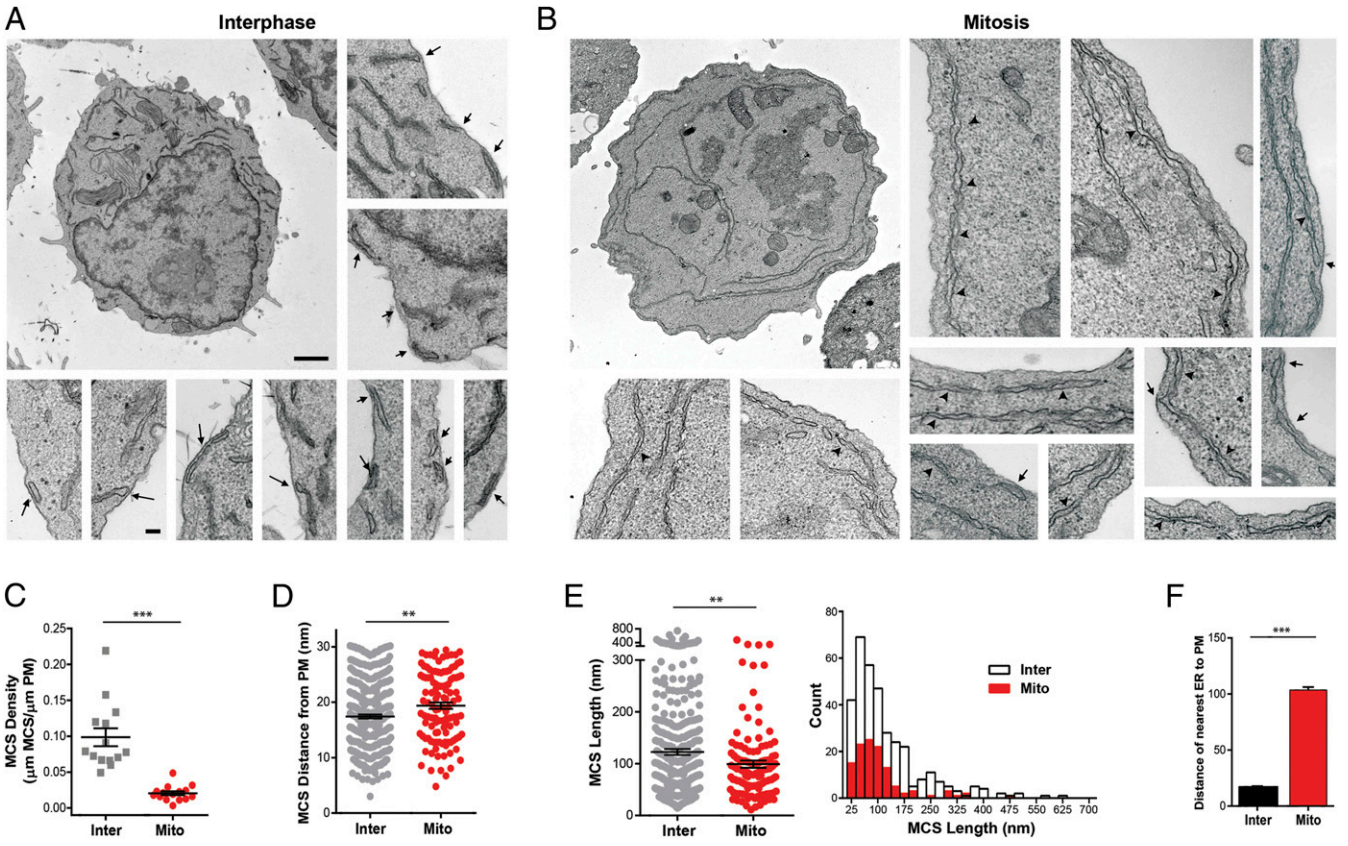


**Fig. 5.** Ultrastructural analysis of ER–PM CS in interphase (Inter) and mitotic (Mito) cells. (*A* and *B*) Representative EM images from Inter (*A*) and Mito (*B*) Jurkat cells. A representative whole cell in shown at low magnification for Inter and Mito, with several zoomed in magnifications of ER–PM CS in Inter (arrows in *A*). For Mito (*B*), in addition to ER–PM CS (arrows), the regions of the closest ER to the PM are shown (arrowheads). (Scale bar: whole-cell images in *A* and *B*, 1 μm; zoomed-in regions in *A* and *B*, 100 nm.) (*C*–*F*) Quantification of ER–PM CS (MCS) density (*C*), junctional gap distance (*D*), and ER–PM CS length (*E*) in Inter and Mito. (*F*) Distance from the closest ER tubules to the PM in high-magnification EM images. For Inter, that distance is by default that of ER–PM CS. $^{**}P \leq 0.01$; $^{***}P \leq 0.001$.

SOCE inhibition, since SOCE is inhibited in primary $CD4^+$ T cells and macrophages in the absence of STIM1 phosphorylation (Fig. 2*B* and *SI Appendix*, Figs. S3*F* and S4*A*). KI mice, where STIM1 was replaced by a nonphosphorylatable STIM1-10A (Fig. 2), are viable and reproduce normally. SOCE is inhibited during mitosis in primary $CD4^+$ T cells isolated from STIM1-10A mice (Fig. 2 *D* and *E*). Collectively, these results show conclusively that STIM1 phosphorylation does not mediate SOCE inhibition in mitosis.

SOCE is activated through direct physical interaction of STIM1 and Orai1, with the stoichiometry of the proteins playing a critical role (52). Maximal SOCE current is observed with an STIM1:Orai1 stoichiometry of 2:1: that is, 12 STIM1 molecules per functional Orai1 hexameric channel. Hence, loss of STIM1 protein in mitosis (~50%) (Fig. 3 *A*–*C* and *SI Appendix*, Fig. S5) is likely to inhibit SOCE even if STIM1 and Orai1 were able to interact across the ER–PM CS.

Interestingly, STIM1 is not degraded through the proteasome pathway in mitosis, as we were unable to detect polyubiquitinated STIM1, even in the presence of a proteasome inhibitor (*SI Appendix*, Fig. S7). Rather, STIM1 targets the autophagy pathway in mitosis, most likely through an interaction with the cochaperone BAG3 (Fig. 3*E*). Autophagy is a conserved process of self-digestion to remove damaged organelles or infectious agents and support energy homeostasis (53). The autophagic flux is higher in early mitosis compared with G1 and G2 (43). BAG3 is a member of the Bcl-2–associated athanogene family that is stimulated under stress and mediates autophagy of cytoskeletal proteins during mitosis (45, 46, 54).

We finally show that the density of ER–PM CSs is reduced in mitosis using MAPPER (Fig. 4) and ultrastructural studies to directly visualize ER–PM CS (Fig. 5). SOCE depends on the integrity of ER–PM CS to allow contact between STIM1 and Orai1. Therefore, the down-regulation of ER–PM junctions in mitosis is likely to be a major contributor to SOCE inhibition by physically preventing STIM1 from interacting with Orai1.

The average distance between the PM and the closest ER in mitosis is ~100 nm (Fig. 5*F*), consistent with a previous EM study on mitotic HeLa cells that showed peripheral ER being excluded from approaching the PM by cortical F-actin at a distance of 150–200 nm (55). In addition, cortical actin contributes to the spatial organization of ER–PM junctions in interphase (56). The actin cortex reorganizes during mitosis to regulate cell surface tension (50, 57). Thus, we speculate that remodeling of the actin cytoskeleton in mitosis contributes to preventing ER–PM cross-talk.

Several studies document ER restructuring in M phase (55, 58–65), suggesting a transition from a tubular structure in interphase cells to a patchy cisternal organization. This report shows a decrease in ER–PM CS in mitosis, which would have implications not only on SOCE and $Ca^{2+}$ signaling but also, on lipid metabolism and membrane structure.

Collectively, our findings provide a comprehensive view of the mechanisms underlying SOCE inhibition in mitosis. They show that cells have enlisted autophagy, protein–protein interaction, and remodeling of ER–PM CS to block $Ca^{2+}$ influx in mitosis. These overlapping mechanisms highlight the critical need to inhibit SOCE to allow for tight regulation of $Ca^{2+}$ dynamics and ensure homeostasis during cell division.

## Materials and Methods

**Mouse Strains.** STIM1-10A-KI mice and control KI mice were generated by Ozgene Pty Ltd. Details are provided in *SI Appendix*. All animals were bred and/or maintained in the Weill Cornell Medicine Qatar pathogen-free animal facility. All experimental procedures and colony maintenance were approved by the Weill Cornell Medicine Institutional Animal Care and Use Committee (protocol 2014–0043).

**Gene Editing of STIM1 in HeLa Cells.** CRISPR-Cas9 was used to introduce monomeric EGFP (A206K) through a short linker (RILQSTVPRARDPPVAT) in frame at the C terminus of one of the STIM1 alleles in HeLa cells (STIM1-EGFP-KI) as described in *SI Appendix, SI Methods*.

**Primary Cell Culture and Cell Lines.** For ex vivo cultured $CD4^+$ T cells, total $CD4^+$ T cells from mouse spleen and lymph nodes were purified using CD4 (L3T4) MicroBeads (Milteny Biotech Inc.). Naïve $CD4^+$ T cells were purified by cell sorting for the $CD4^+CD62L^+CD25^-$ population. $CD4^+$ T cells were stimulated with plate-bound anti-CD3 (145-2C11) and anti-CD28 (37.51) antibodies and cultured in neutralizing condition ($Th_{neu}$) in the presence of 50 U/mL human interleukin-2 (PeproTech) as previously described (66).

YFP-HA-hOrai1 stable CHO cells were described previously (34). STIM1-knockout MEF cells were a gift from Masatsugu Oh-hora, Tokyo Medical and Dental University, Tokyo (48). To generate hSTIM1-YFP stable STIM1-knockout MEF cells, STIM1-KO-MEF cells were infected with retrovirus expressing hSTIM1-YFP (19754; Addgene) and then, selected using puromycin.

To generate HEK293 and STIM1-EGFP-KI HeLa cell lines stably expressing the mitotic marker H2B-RFP, cells were infected with lentivirus expressing H2B-RFP (26001; Addgene) (67). H2B-RFP–expressing cells were enriched for the $RFP^+$ population on a cell sorter (BD FACSAria II).

To generate GFP-LC3 stable HEK293 cells, cells were infected with retrovirus expressing GFP-LC3 (22405; Addgene) (68) and then, enriched for the $GFP^+$ population (BD FACSAria II).

For mitotic synchronization, cells were treated with 100 ng/mL nocodazole (Sigma) for 16–18 h. For the experiments assessing STIM1 ubiquitination, HEK293 and Jurkat cells were treated with nocodazole for 16 h followed by incubation with 25 μM MG-132 (Selleckchem) for an additional 4 h.

**Plasmids.** YFP-Bag3 plasmid (EX-U1468-M15) was purchased from GeneCopoeia. YFP-CAD (33) and mCherry-STIM1 (69) plasmids were a gift from Rich Lewis, Stanford University, Stanford, CA, and the YFP-STIM1-482 plasmid (25) was a gift from James Putney, NIH, Bethesda, MD.

To construct human STIM1-10A (S486A, S492A, S575A, S600A, S608A, S618A, S621A, T626A, S628A, S668A) and STIM1-10E mutant, pSGEM-mCherry-STIM1-7A and pSGEM-mCherry-STIM1-7E plasmids (29) were used as templates for site-directed mutagenesis of S575, S600, and S608 for either A or E substitution using the Quickchange mutagenesis kit (Agilent Technologies). The primer pairs used are listed in *SI Appendix*.

**Cell Sorting and FACS Analysis.** To isolate the G2/M population from nocodazole-treated, ex vivo-cultured $CD4^+$ T cells (mitotic $CD4^+$ T cells), cells were stained with either NuclearID Red for $Ca^{2+}$ imaging or Hoechst33342 for Western blots and MS. Cells were sorted on an FACSAriaII (BD Biosciences) and collected into a medium containing nocodazole. Jurkat cells were stained with Hoechst33342 and analyzed for cell cycle profile on a BD Fortessa. When the G2/M population was above 85% of total cells, cells were used for additional analysis. Mitotic HEK293 cells were obtained by nocodazole treatment followed by mitotic shake off.

To isolate asynchronous and mitotic HEK293 cells expressing mCherry-STIM1-WT or mCherry-STIM1-10A for $Ca^{2+}$ imaging, asynchronous and mitotic shake-off cells transiently expressing mCherry-STIM1-WT or -10A were subjected to cell sorting for the $mCherry^+$ population. Cells were collected into the medium containing nocodazole.

For cell viability analysis, cells were stained with Fixable Viability Dyes eFluor 506 (ThermoFisher), fixed, permeabilized, and stained with Alexa Fluor 647 Rat antihistone H3 (pS28) antibody (clone HTA28; 558217; BD), a well-known marker for mitosis (70). eFluor 506 permeates only dead cells with a damaged PM and is not viable with an intact PM. It further increases its fluorescence dramatically on binding cellular proteins, thus allowing differentiation between the live and dead cell populations. The dye is fixable, allowing retention of the fluorescence before additional processing.

For localization analysis, cells were harvested and stained with Fixable Viability Dyes eFluor 506 (ThermoFisher) and mouse anti-HA antibody (901502; BioLegend) follow by staining with secondary Goat anti-Mouse Alexa Fluor 405 (ThermoFisher Scientific) before fixation. Flow cytometry data were analyzed by the FlowJo v10 software (Tree Star).

**Confocal Microscopy.** Cells were cultured on 35-mm glass-bottom dishes (MatTek) at 37 °C with 5% $CO_2$ and imaged in Ringer solution containing 155 mM NaCl, 4.5 mM KCl, 2 mM $CaCl_2$, 1 mM $MgCl_2$, 10 mM D-glucose, and 5 mM Na-Hepes, pH 7.4. For $Ca^{2+}$-free Ringer, $CaCl_2$ was replaced with $MgCl_2$. Imaging was performed on a Zeiss LSM 880 confocal microscope using a Plan Apo 63×/1.4 oil DIC II objective with pinhole 1AU or fully open as indicated.

Antibodies and reagents used for staining were STIM1 N-terminal rabbit polyclonal antibody (11565–1-AP; lot no. 00016319; Proteintech), α-tubulin mAb (Cell Signaling), HA mAb (901502; BioLegend), Alexa Fluor 633 goat anti-mouse IgG antibodies, and phalloidin Alexa Fluor 633 (Invitrogen).

Images were analyzed using ZEN Black software, and figures were compiled using Adobe Photoshop or Illustrator; 3D reconstruction of confocal stacks and ER–PM junction analysis were performed using the Imaris package (Bitplane).

**TIRF and Epifluorescence Imaging.** Live cell TIRF and epifluorescence imaging were performed on a Zeiss Z1 AxioObserver inverted fluorescence microscope with a TIRF slider using an alpha Plan-Apochromat 63×/1.46 Oil Corr M27 TIRF objective at 37 °C. Images were processed using Zeiss Zen Blue software.

**$Ca^{2+}$ Imaging.** Thapsigargin, ionomycin, and Fura2-AM were purchased from Invitrogen. Equal numbers of cells were loaded with Fura2-AM for 30 min at 37 °C, washed with $Ca^{2+}$-free Ringer solution (120 mM NaCl, 5 mM KCl, 3 mM $MgCl_2$, 20 mM Hepes, pH 7.4), and transferred into the glass-bottom 96-well plate (3603; Corning Costar). The plate was centrifuged at 1,109 × *g* for 3 min at room temperature. $Ca^{2+}$ imaging was performed on a FlexStation 3 Multi-Mode Microplate Reader (Molecular Devices) by recording fluorescence (>500 nm) after alternate excitation at 340 and 380 nm (71). SOCE was calculated by subtracting fluorescence values (F340/F380) before $Ca^{2+}$ addition from the highest value after restoration of extracellular $Ca^{2+}$. Graphs were analyzed in Prism 6 software (GraphPad).

**MS.** Samples were analyzed by liquid chromatography–tandem MS using an analytical platform consisting of an EASY nLC-1200 interfaced to a Q-Exactive HF orbitrap mass spectrometer (ThermoFisher). MS raw data were searched using the MaxQuant suite of algorithms (72, 73) (version 1.5.2.80) against the *Homo sapiens* UniprotKB database (canonical and isoforms; as 20151012; 48460) (74) using default parameters with carbamidomethylated cysteine as fixed and acetyl protein N termini, oxidated methionine, and phosphorylated serine/threonine/tyrosine as fixed and variable post-translational modifications, respectively. The false discovery rate was controlled on the peptide and protein as well as modification site level to 1% by the reverse database approach (75, 76).

**EM.** Cell pellets were fixed with a modified Karmovsky's fix (2.5% glutaraldehyde, 2% parafomaldehyde in 0.1 M sodium Sorenson's phosphate buffer at pH 7.4) and a secondary fixation in reduced osmium tetroxide (77). After en bloc staining with uranyl acetate and graded ethanol dehydration, samples were embedded in an Epon analog resin. Ultrathin sections (65 nm) were contrasted with lead citrate (78) and viewed on a JEM 1400 electron microscope (JEOL, USA, Inc.) operated at 100 kV. Digital images were captured on a Veleta 2K × 2K CCD camera (Olympus-SIS).

**Statistics.** Data are presented as mean ± SEM. Groups were compared using the Prism 6 software (GraphPad) using either paired or unpaired two-tailed Student *t* test or the Wilcoxon nonparametric test as indicated. Statistical significance is indicated by *P* values.

**ACKNOWLEDGMENTS.** We thank colleagues who shared valuable reagents: Stefan Feske (New York University) for the STIM1flox/flox mouse line; Masatsugu Oh-hora (Tokyo Medical and Dental University) for the STIM1 KO MEF cell line; Richard S. Lewis (Stanford) for the mCherry-STIM1, YFP-HA-Orai1ΔC, and YFP-CAD plasmids; Jen Liou (University of Texas Southwestern) for GFP-MAPPER; and Jim Putney (NIH) for YFP-STIM1-482 plasmid. We thank the Microscopy Core; Neha Goswani and Hisham Ben Hamidane at the Proteomic Core; the vivarium core staff at Weill Cornell Medicine Qatar (WCM-Q); and Lee Cohen-Gould at the imaging core at Weill Cornell Medicine for their technical support. We also thank Ms. Aleksandra Liberska for help with the cell-sorting studies. This work and the WCM-Q Cores were supported by the Biomedical Research Program at the WCM-Q, a program funded by Qatar Foundation. S.C. and C.W.T. were supported by Wellcome Senior Investigator Award 101844 (to C.W.T.). The statements made herein are solely the responsibility of the authors.

1. Levine MS, Holland AJ (2018) The impact of mitotic errors on cell proliferation and tumorigenesis. *Genes Dev* 32:620–638.
2. Nigg EA (1993) Targets of cyclin-dependent protein kinases. *Curr Opin Cell Biol* 5:187–193.
3. Whitaker M (2006) Calcium at fertilization and in early development. *Physiol Rev* 86: 25–88.
4. Ciapa B, Pesando D, Wilding M, Whitaker M (1994) Cell-cycle calcium transients driven by cyclic changes in inositol trisphosphate levels. *Nature* 368:875–878.
5. Groigno L, Whitaker M (1998) An anaphase calcium signal controls chromosome disjunction in early sea urchin embryos. *Cell* 92:193–204.
6. Kao JP, Alderton JM, Tsien RY, Steinhardt RA (1990) Active involvement of $Ca^{2+}$ in mitotic progression of Swiss 3T3 fibroblasts. *J Cell Biol* 111:183–196.
7. Tombes RM, Simerly C, Borisy GG, Schatten G (1992) Meiosis, egg activation, and nuclear envelope breakdown are differentially reliant on $Ca^{2+}$, whereas germinal vesicle breakdown is $Ca^{2+}$ independent in the mouse oocyte. *J Cell Biol* 117:799–811.
8. Wilding M, Wright EM, Patel R, Ellis-Davies G, Whitaker M (1996) Local perinuclear calcium signals associated with mitosis-entry in early sea urchin embryos. *J Cell Biol* 135:191–199.
9. Sun L, Machaca K (2004) Ca(2+)(cyt) negatively regulates the initiation of oocyte maturation. *J Cell Biol* 165:63–75.
10. Sun L, et al. (2008) $Ca^{2+}$ homeostasis regulates *Xenopus* oocyte maturation. *Biol Reprod* 78:726–735.
11. Machaca K (2007) $Ca^{2+}$ signaling differentiation during oocyte maturation. *J Cell Physiol* 213:331–340.
12. Nader N, Kulkarni RP, Dib M, Machaca K (2013) How to make a good egg!: The need for remodeling of oocyte Ca($^{2+}$) signaling to mediate the egg-to-embryo transition. *Cell Calcium* 53:41–54.
13. Arredouani A, Yu F, Sun L, Machaca K (2010) Regulation of store-operated $Ca^{2+}$ entry during the cell cycle. *J Cell Sci* 123:2155–2162.
14. Prakriya M, Lewis RS (2015) Store-operated calcium channels. *Physiol Rev* 95:1383–1436.
15. Lacruz RS, Feske S (2015) Diseases caused by mutations in ORAI1 and STIM1. *Ann N Y Acad Sci* 1356:45–79.
16. Wu MM, Buchanan J, Luik RM, Lewis RS (2006) Ca2+ store depletion causes STIM1 to accumulate in ER regions closely associated with the plasma membrane. *J Cell Biol* 174:803–813.
17. Chang CL, Chen YJ, Liou J (2017) ER-plasma membrane junctions: Why and how do we study them? *Biochim Biophys Acta Mol Cell Res* 1864:1494–1506.
18. Saheki Y, De Camilli P (2017) Endoplasmic reticulum-plasma membrane contact sites. *Annu Rev Biochem* 86:659–684.
19. Wu H, Carvalho P, Voeltz GK (2018) Here, there, and everywhere: The importance of ER membrane contact sites. *Science* 361:eaan5835.
20. Preston SF, Sha'afi RI, Berlin RD (1991) Regulation of $Ca^{2+}$ influx during mitosis: $Ca^{2+}$ influx and depletion of intracellular $Ca^{2+}$ stores are coupled in interphase but not mitosis. *Cell Regul* 2:915–925.
21. Machaca K, Haun S (2000) Store-operated calcium entry inactivates at the germinal vesicle breakdown stage of Xenopus meiosis. *J Biol Chem* 275:38710–38715.
22. Machaca K, Haun S (2002) Induction of maturation-promoting factor during Xenopus oocyte maturation uncouples Ca($^{2+}$) store depletion from store-operated Ca($^{2+}$) entry. *J Cell Biol* 156:75–85.
23. Russa AD, et al. (2008) Microtubule remodeling mediates the inhibition of store-operated calcium entry (SOCE) during mitosis in COS-7 cells. *Arch Histol Cytol* 71:249–263.
24. Tani D, Monteilh-Zoller MK, Fleig A, Penner R (2007) Cell cycle-dependent regulation of store-operated $I_{(CRAC)}$ and $Mg^{2+}$-nucleotide-regulated MagNuM (TRPM7) currents. *Cell Calcium* 41:249–260.
25. Smyth JT, et al. (2009) Phosphorylation of STIM1 underlies suppression of store-operated calcium entry during mitosis. *Nat Cell Biol* 11:1465–1472.
26. Lee B, Palermo G, Machaca K (2013) Downregulation of store-operated $Ca^{2+}$ entry during mammalian meiosis is required for the egg-to-embryo transition. *J Cell Sci* 126: 1672–1681.
27. Sun L, Haun S, Jones RC, Edmondson RD, Machaca K (2009) Kinase-dependent regulation of inositol 1,4,5-trisphosphate-dependent Ca2+ release during oocyte maturation. *J Biol Chem* 284:20184–20196.
28. Yu F, Sun L, Machaca K (2010) Constitutive recycling of the store-operated $Ca^{2+}$ channel Orai1 and its internalization during meiosis. *J Cell Biol* 191:523–535.
29. Yu F, Sun L, Machaca K (2009) Orai1 internalization and STIM1 clustering inhibition modulate SOCE inactivation during meiosis. *Proc Natl Acad Sci USA* 106:17401–17406.
30. Cheon B, Lee HC, Wakai T, Fissore RA (2013) $Ca^{2+}$ influx and the store-operated $Ca^{2+}$ entry pathway undergo regulation during mouse oocyte maturation. *Mol Biol Cell* 24: 1396–1410.
31. Smyth JT, Beg AM, Wu S, Putney JW, Jr, Rusan NM (2012) Phosphoregulation of STIM1 leads to exclusion of the endoplasmic reticulum from the mitotic spindle. *Curr Biol* 22:1487–1493.
32. Yuan JP, et al. (2009) SOAR and the polybasic STIM1 domains gate and regulate Orai channels. *Nat Cell Biol* 11:337–343.
33. Park CY, et al. (2009) STIM1 clusters and activates CRAC channels via direct binding of a cytosolic domain to Orai1. *Cell* 136:876–890.
34. Hodeify R, et al. (2015) A STIM1-dependent 'trafficking trap' mechanism regulates Orai1 plasma membrane residence and $Ca^{2+}$ influx levels. *J Cell Sci* 128:3143–3154.
35. Shibata K, Inagaki M, Ajiro K (1990) Mitosis-specific histone H3 phosphorylation in vitro in nucleosome structures. *Eur J Biochem* 192:87–93.
36. Pozo-Guisado E, et al. (2010) Phosphorylation of STIM1 at ERK1/2 target sites modulates store-operated calcium entry. *J Cell Sci* 123:3084–3093.
37. Ong HL, et al. (2015) STIM2 enhances receptor-stimulated $Ca^{2+}$ signaling by promoting recruitment of STIM1 to the endoplasmic reticulum-plasma membrane junctions. *Sci Signal* 8:ra3.
38. Giordano F, et al. (2013) PI(4,5)P(2)-dependent and Ca($^{2+}$)-regulated ER-PM interactions mediated by the extended synaptotagmins. *Cell* 153:1494–1509.
39. Besprozvannaya M, et al. (2018) GRAM domain proteins specialize functionally distinct ER-PM contact sites in human cells. *eLife* 7:e31019.

40. Ghai R, et al. (2017) ORP5 and ORP8 bind phosphatidylinositol-4, 5-biphosphate (PtdIns(4,5)P $_2$) and regulate its level at the plasma membrane. *Nat Commun* 8:757.
41. Sohn M, et al. (2018) PI(4,5)$P_2$ controls plasma membrane PI4P and PS levels via ORP5/8 recruitment to ER-PM contact sites. *J Cell Biol* 217:1797–1813.
42. Keil JM, Shen Z, Briggs SP, Patrick GN (2010) Regulation of STIM1 and SOCE by the ubiquitin-proteasome system (UPS). *PLoS One* 5:e13465.
43. Li Z, Ji X, Wang D, Liu J, Zhang X (2016) Autophagic flux is highly active in early mitosis and differentially regulated throughout the cell cycle. *Oncotarget* 7:39705–39718.
44. Yamamoto A, et al. (1998) Bafilomycin A1 prevents maturation of autophagic vacuoles by inhibiting fusion between autophagosomes and lysosomes in rat hepatoma cell line, H-4-II-E cells. *Cell Struct Funct* 23:33–42.
45. Fuchs M, et al. (2015) A role for the chaperone complex BAG3-HSPB8 in actin dynamics, spindle orientation and proper chromosome segregation during mitosis. *PLoS Genet* 11:e1005582.
46. Behl C (2016) Breaking BAG: The Co-chaperone BAG3 in health and disease. *Trends Pharmacol Sci* 37:672–688.
47. Hoover PJ, Lewis RS (2011) Stoichiometric requirements for trapping and gating of Ca2+ release-activated Ca2+ (CRAC) channels by stromal interaction molecule 1 (STIM1). *Proc Natl Acad Sci USA* 108:13299–13304.
48. Oh-Hora M, et al. (2008) Dual functions for the endoplasmic reticulum calcium sensors STIM1 and STIM2 in T cell activation and tolerance. *Nat Immunol* 9:432–443.
49. Jongsma ML, Berlin I, Neefjes J (2015) On the move: Organelle dynamics during mitosis. *Trends Cell Biol* 25:112–124.
50. Stewart MP, et al. (2011) Hydrostatic pressure and the actomyosin cortex drive mitotic cell rounding. *Nature* 469:226–230.
51. Chang CL, et al. (2013) Feedback regulation of receptor-induced Ca2+ signaling mediated by E-Syt1 and Nir2 at endoplasmic reticulum-plasma membrane junctions. *Cell Rep* 5:813–825.
52. Yen M, Lewis RS (2019) Numbers count: How STIM and Orai stoichiometry affect store-operated calcium entry. *Cell Calcium* 79:35–43.
53. Yang Z, Klionsky DJ (2010) Eaten alive: A history of macroautophagy. *Nat Cell Biol* 12:814–822.
54. Rosati A, Graziano V, De Laurenzi V, Pascale M, Turco MC (2011) BAG3: A multifaceted protein that regulates major cell pathways. *Cell Death Dis* 2:e141.
55. McCullough S, Lucocq J (2005) Endoplasmic reticulum positioning and partitioning in mitotic HeLa cells. *J Anat* 206:415–425.
56. Hsieh TS, Chen YJ, Chang CL, Lee WR, Liou J (2017) Cortical actin contributes to spatial organization of ER-PM junctions. *Mol Biol Cell* 28:3171–3180.
57. Chugh P, et al. (2017) Actin cortex architecture regulates cell surface tension. *Nat Cell Biol* 19:689–697.
58. Campanella C, Andreuccetti P, Taddei C, Talevi R (1984) The modifications of cortical endoplasmic reticulum during in vitro maturation of Xenopus laevis oocytes and its involvement in cortical granule exocytosis. *J Exp Zool* 229:283–293.
59. Charbonneau M, Grey RD (1984) The onset of activation responsiveness during maturation coincides with the formation of the cortical endoplasmic reticulum in oocytes of Xenopus laevis. *Dev Biol* 102:90–97.
60. Jaffe LA, Terasaki M (1994) Structural changes in the endoplasmic reticulum of starfish oocytes during meiotic maturation and fertilization. *Dev Biol* 164:579–587.
61. Mehlmann LM, Mikoshiba K, Kline D (1996) Redistribution and increase in cortical inositol 1,4,5-trisphosphate receptors after meiotic maturation of the mouse oocyte. *Dev Biol* 180:489–498.
62. Shiraishi K, et al. (1995) Developmental changes in the distribution of the endoplasmic reticulum and inositol 1,4,5-trisphosphate receptors and the spatial pattern of Ca2+ release during maturation of hamster oocytes. *Dev Biol* 170:594–606.
63. Terasaki M, Runft LL, Hand AR (2001) Changes in organization of the endoplasmic reticulum during Xenopus oocyte maturation and activation. *Mol Biol Cell* 12:1103–1116.
64. Lu L, Ladinsky MS, Kirchhausen T (2009) Cisternal organization of the endoplasmic reticulum during mitosis. *Mol Biol Cell* 20:3471–3480.
65. Poteryaev D, Squirrell JM, Campbell JM, White JG, Spang A (2005) Involvement of the actin cytoskeleton and homotypic membrane fusion in ER dynamics in Caenorhabditis elegans. *Mol Biol Cell* 16:2139–2153.
66. Yu F, Sharma S, Edwards J, Feigenbaum L, Zhu J (2015) Dynamic expression of transcription factors T-bet and GATA-3 by regulatory T cells maintains immunotolerance. *Nat Immunol* 16:197–206.
67. Beronja S, Livshits G, Williams S, Fuchs E (2010) Rapid functional dissection of genetic networks via tissue-specific transduction and RNAi in mouse embryos. *Nat Med* 16:821–827.
68. Fung C, Lock R, Gao S, Salas E, Debnath J (2008) Induction of autophagy during extracellular matrix detachment promotes cell survival. *Mol Biol Cell* 19:797–806.
69. Luik RM, Wu MM, Buchanan J, Lewis RS (2006) The elementary unit of store-operated Ca2+ entry: Local activation of CRAC channels by STIM1 at ER-plasma membrane junctions. *J Cell Biol* 174:815–825.
70. Hirata A, et al. (2004) Characterization of a monoclonal antibody, HTA28, recognizing a histone H3 phosphorylation site as a useful marker of M-phase cells. *J Histochem Cytochem* 52:1503–1509.
71. Tovey SC, Sun Y, Taylor CW (2006) Rapid functional assays of intracellular Ca2+ channels. *Nat Protoc* 1:259–263.
72. Cox J, Mann M (2008) MaxQuant enables high peptide identification rates, individualized p.p.b.-range mass accuracies and proteome-wide protein quantification. *Nat Biotechnol* 26:1367–1372.
73. Cox J, et al. (2011) Andromeda: A peptide search engine integrated into the MaxQuant environment. *J Proteome Res* 10:1794–1805.
74. UniProt Consortium (2008) The universal protein resource (UniProt). *Nucleic Acids Res* 36:D190–D195.
75. Peng J, Elias JE, Thoreen CC, Licklider LJ, Gygi SP (2003) Evaluation of multidimensional chromatography coupled with tandem mass spectrometry (LC/LC-MS/MS) for large-scale protein analysis: The yeast proteome. *J Proteome Res* 2:43–50.
76. Elias JE, Gygi SP (2007) Target-decoy search strategy for increased confidence in large-scale protein identifications by mass spectrometry. *Nat Methods* 4:207–214.
77. de Bruijn WC (1973) Glycogen, its chemistry and morphologic appearance in the electron microscope. I. A modified OsO 4 fixative which selectively contrasts glycogen. *J Ultrastruct Res* 42:29–50.
78. Venable JH, Coggeshall R (1965) A simplified lead citrate stain for use in electron microscopy. *J Cell Biol* 25:407–408.